JCTC Journal of Chemical Theory and Computation

pubs.acs.org/JCTC Article

Ab Initio-Based Modeling of Thermodynamic Cyclic Voltammograms: A Benchmark Study on Ag(100) in Bromide Solutions

Nicolas Bergmann, Nicolas G. Hörmann,* and Karsten Reuter

Cite This: J. Chem. Theory Comput. 2023, 19, 8815−8825 Read Online

ABSTRACT: Experimental cyclic voltammograms (CVs) measured in the slow scan rate limit can be entirely described in terms of the thermodynamic equilibrium quantities of the electrified solid−liquid interface. They correspondingly serve as an important benchmark for the quality of first-principles calculations of interfacial thermodynamics. Here, we investigate the partially drastic approximations made presently in computationally efficient calculations for the well-defined showcase of an Ag(100) model electrode in Br-containing electrolytes, where the nontrivial part of the CV stems from the electrosorption of Br ions. We specifically study the entanglement of common approximations in the treatment of solvation and field effects, as well as in the way macroscopic averages of the two key quantities, namely, the potential-dependent adsorbate coverage and electrosorption valency, are derived from the first-principles energetics. We demonstrate that the combination of energetics obtained within an implicit solvation model and a perturbative second order account of capacitive double layer effects with a constant-potential grand-canonical Monte Carlo sampling of the adsorbate layer provides an accurate description of the experimental CV. However, our analysis also shows that error cancellation at lower levels of theory may equally lead to good descriptions even though key underlying physics such as the disorder−order transition of the Br adlayer at increasing coverages is inadequately treated.

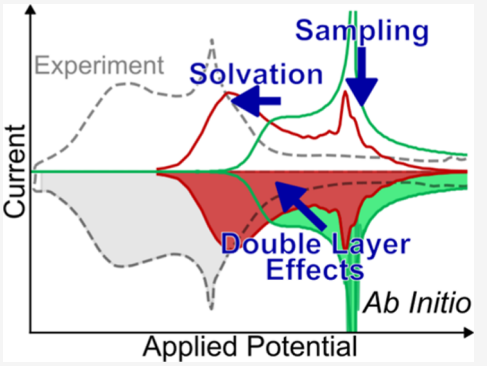

1. INTRODUCTION

Cyclic voltammetry is a widely employed electrochemical experiment to characterize electrocatalytic processes occurring at electrified solid−liquid interfaces.[1,2] A cyclic voltammogram (CV) records the electric current j observed while sweeping an applied electrode potential ϕ_E at a constant scan rate ν upward and downward within a given potential window.[3−6] Peaks in the resulting voltammogram $j(\phi_E)$ are then interpreted as fingerprints of occurring electrochemical reactions,[5] whose fundamental nature can experimentally be uncovered by, e.g., investigating the CV's dependencies on pH, applied potential limits, scan rate, or the electrolyte's chemical composition.[7,8] The derived assignments are often not unambiguous though and could strongly benefit from independent and predictive-quality computational modeling. Whenever diffusion limitations are absent, CV currents ($j = d\sigma/dt$) within the stable potential window of the electrolyte directly relate to changes in the equilibrium electronic surface charge $d\sigma$, due to differential electrode potential changes $d\phi_E$ induced by the constant scan rate $\nu = d\phi_E/dt$. In this case, the dominant charging processes are the polarization of the electrolyte solution via double layer (DL) charging ($d\sigma_{DL}$) and Faradaic processes, in which charged particles transfer across the electrode. In the defined case of a stable model electrode surface that neither reconstructs nor dissolves, on which we will focus here, the electronic charge transfer ($d\sigma_a$) due to the latter processes stems entirely from electrosorption of adsorbates a onto the surface.[5,9,10] $d\sigma_a$ is then given by the change in adsorbate coverage θ_a multiplied by the number of exchanged electrons per adsorbate, aka the electrosorption valency l_a.[11,12] One can thus formally write

$$j(\phi_E) = \nu \frac{d\sigma_{DL}}{d\phi_E} + \nu l_a(\theta_a, \phi_E) \frac{d\theta_a}{d\phi_E}. \quad (1)$$

With $\sigma_{DL}(\phi_E)$ often a quasi-constant baseline current, the theoretical modeling of a CV correspondingly requires an accurate description of the coverage versus potential relation $\theta_a(\phi_E)$, as well as an appropriate consideration of the electrosorption valency $l_a(\theta_a, \phi_E)$. In the slow scan rate limit, both of these quantities are thermodynamic equilibrium quantities. In this respect, the corresponding experimental

Received: August 31, 2023
Revised: November 11, 2023
Accepted: November 17, 2023
Published: December 1, 2023

https://doi.org/10.1021/acs.jctc.3c00957
J. Chem. Theory Comput. 2023, 19, 8815−8825

CVs also serve as important benchmarks for the quality of theoretical predictions of the interfacial thermodynamics.

It is with this motivation to benchmark various prevalent thermodynamic modeling choices and approximations that we here study the CV of a Ag(100) electrode in a Br^--containing electrolyte. This is a suitable and experimentally well-studied prototype system,[13−15] for which high-quality CVs are available and in which electronic charge transfer arises from the electrosorption of Br^- ions onto defined high-symmetry sites of an otherwise rigid Ag(100) lattice. We specifically compare popular choices made in three significant modeling steps: the modeling of the liquid−solid interface, the determination of the energetics at applied potential conditions, and the statistical mechanics description are used to obtain macroscopic averages of l_a and θ_a from the atomistic energetics. The focus is thereby on computationally efficient approaches based on density-functional theory (DFT) calculations using a slab model for the electrode and without explicit representation of the electrolyte solution. We thus compare vacuum calculations to those in an implicit solvent environment, consider applied potential effects in first and second order,[16,17] and apply mean-field and lattice-based grand-canonical Monte Carlo (GC-MC) sampling.[10,14] The analysis shows that only higher order thermodynamics coupled to the lattice GC-MC sampling consistently recreates the characteristic peak shape and integral of the experimental CVs for the right reasons.

2. EXPERIMENTAL CVS OF AG(100) IN BROMIDE SOLUTIONS

The model system Ag(100) in Br^--containing electrolytes and its CV has been studied extensively.[13−15,20−24] Figure 1 shows a collection of digitized experimental CVs, using the echemdb database.[18] The CVs span a range of electrolyte concentrations and cations. CVs with concentrations above 10 mM exhibit no significant hysteresis, i.e., the peak positions in the anodic sweep direction are essentially identical to those of the cathodic sweep direction, indicating the thermodynamic character of the experiments.[5] Kinetic limitations, likely due to Br^- diffusion,[19] only become relevant at much smaller concentrations (bold, red curve in Figure 1), which will not be studied here.

In general, the "butterfly"-shape of the CV is characterized by a first shoulder (peak P1) at lower potentials, which is ascribed to the formation of a disordered Br-adlayer with $\theta_{Br} \leq$ 0.3 monolayer (ML), as evidenced in surface X-ray scattering experiments by Wandlowski et al.[13] The prominent sharp peak (P2) at ≈0.38 ML, i.e., ∼75% of the limiting coverage 0.5 ML, marks the second order disorder−order phase transition where phase boundaries between different sublattices of Br adlayers are continuously removed,[25,26] ultimately resulting in an ordered $c(2 \times 2)$ Br adlayer with 0.5 ML coverage at high potentials.[13,14,20]

The total transferred electronic charge σ_{Br}, as determined by integrating the CV without baseline currents (red shaded area in Figure 1), indicates that the electrosorption valency is a noninteger. Assuming a nominal full electron transfer during electrosorption of Br^-, i.e., $l_{Br} = -1$, the expected transferred electronic charge to a 0.5 ML adlayer would be $\sigma_{Br,\,nominal} = 94\ \mu C/cm^2$. This is 25% higher than the actually measured value of $\sigma_{Br} \approx 70\ \mu C/cm^2$, cf. Figure 1. Additionally, ref 13 reported a non-Nernstian potential shift of the P2 peak of 110 meV per decadic logarithm of the Br^- concentration. Both of these observations are consistent with a noninteger electrosorption valency $l_{Br} \sim -0.75$, where l_{Br} is defined as[11]

$$l_{Br} = -\frac{1}{e}\left(\frac{\partial \sigma_{Br}}{\partial \theta_{Br}}\right)_{\phi_E} = -\frac{1}{e}\frac{\left(\frac{\partial \theta_{Br}}{\partial \phi_E}\right)_{\tilde{\mu}_{Br^-}}}{\left(\frac{\partial \theta_{Br}}{\partial \tilde{\mu}_{Br^-}}\right)_{\phi_E}}, \tag{2}$$

where e is the elementary charge and $\tilde{\mu}_{Br^-}$ is the Br^- electrochemical potential. While not further discussed here, the known interdependencies of electrosorption valency and CV peak shapes[27] indicate that this nonideal l_{Br} value might as well explain the cation-dependence of the peak shape and integral observed in ref 15.

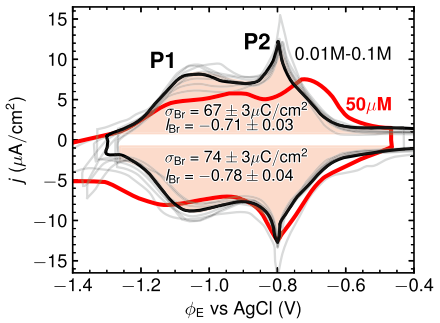

Figure 1. Ten experimental CVs of Ag(100) in Br^--containing electrolytes (gray lines) obtained from the echemdb database,[18] with ν- and c_{Br^-}-normalized to 50 mV/s and 0.1 M, respectively. The CV measured by Nakamura et al.[15] (bold black line) is henceforth taken as representative experimental reference in all figures below. In the anodic sweep direction, P1 marks the CV peak corresponding to the onset of Br electrosorption. At P2, the second order disorder−order phase transition occurs to the final $c(2 \times 2)$ Br-covered surface. Integrating the CV over the potential range from [−1.3 V, −0.4 V] vs AgCl (indicated by the red shaded area) and subtracting the capacitive DL baseline current contribution yields the total transferred electrosorption charge σ_{Br} and derived from it the electrosorption valency l_{Br} in the anodic and the cathodic sweep direction. The values quoted in the figure correspond to the average and standard deviation over the 10 CVs. The 10 CVs are from measurements at higher electrolyte concentrations (0.01−0.1 M), where thermodynamic CVs can be obtained at the applied scan rates. This is contrasted by the CV shown as a red line that was measured at $c_{Br^-} = 50\ \mu M$.[19] In this curve, Br^- electrosorption's kinetic limitations become visible through the peak hysteresis between the anodic and cathodic sweep directions. See the Supporting Information for the individual CVs and their references as well as all details regarding the CV normalization and integration.

3. THEORY

While computing CVs with effective models, e.g., mean-field or lattice Hamiltonians, based on fitted experimental parameters has a long tradition,[14,23,28] theoretical descriptions determined from first-principles methods based on DFT calculations are comparably recent.[9,16] A typical simulation workflow for such ab initio thermodynamic CV modeling approaches is depicted in Figure 2. In the present work, we assess the impact of various choices at each of the modeling steps.

In the first step, we determine the DFT energetics of a range of adsorbate structures in a given solvent environment, considering prevalent approximations of the latter in the form of vacuum and an implicit solvent. Subsequently, we evaluate the relative stability of these structures as a function of

https://doi.org/10.1021/acs.jctc.3c00957
J. Chem. Theory Comput. 2023, 19, 8815−8825

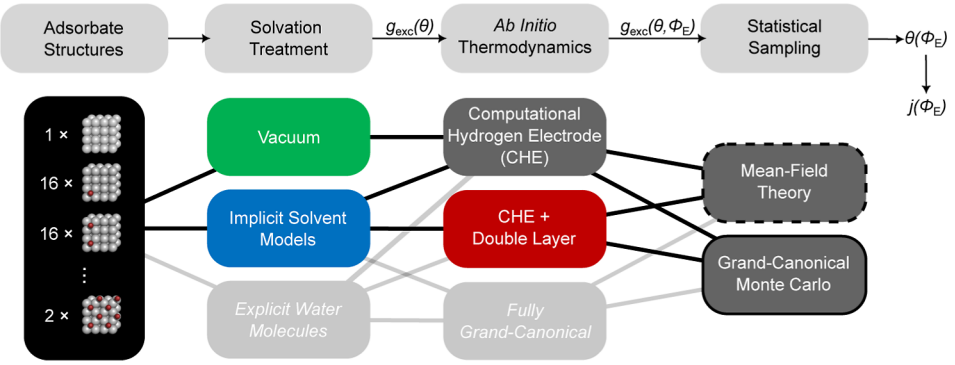

Figure 2. Typical modeling steps to derive thermodynamic CVs from first-principles calculations include the construction of a range of adsorbate structures on an electrode (shown in the left panel from the top view) in a chosen solvent environment, the assessment of their stability using an ab initio thermodynamics approach, and finally the determination of macroscopic averages via statistical sampling. The color codes and line forms of the different boxes reflect the colors used for corresponding data in all Figures below. While included in this schematic, we do not further consider simulations with explicit water molecules and with fully grand canonical ab initio thermodynamics due to their high computational cost.

electron and ion electrochemical potentials within an ab initio thermodynamics framework. Finally, we perform thermodynamic averaging to obtain the macroscopic averages of θ_{Br} and l_{Br}. Using eq 1, this then yields the computed CV curve, where we disregard the essentially structureless baseline current contribution σ_{DL} that was also approximately removed from the experimental CVs.

3.1. Adsorbate Structures. Br is experimentally known to adsorb onto the 4-fold hollow sites of Ag(100) with a maximum coverage of 0.5 ML in a regular $c(2 \times 2)$ arrangement as consistent with high nearest-neighbor (NN) repulsions.[22] We correspondingly construct a systematic data set of adsorbate structures by enumerating all configurations in a (4×4) Ag(100) surface unit-cell that do not exhibit NN occupations.[14] In total, this yielded 28 symmetrically unique structures. To include information about the strong NN interactions in the data set, we add a single 9/16 ML structure with one additional Br on an empty site of the $c(2 \times 2)$ structure.

3.2. Computational Method and Solvation Treatment. Different levels of theory exist to model the solid−liquid interface.[29] In principle, the most precise ab initio method uses explicit electrolyte and solvent molecules. These calculations can model effects such as hydrogen bonding networks toward surface adsorbates,[30] potential-dependent solvent orientation, and concomitant capacitive responses,[31,32] as well as electronic effects of the solid−liquid interface.[33,34] However, the realistic treatment of the electrolyte solution requires significant computational resources, due to the necessity of performing molecular dynamic simulations, especially with the appropriate inclusion of the electrode potential.[30−32]

We therefore focus on a simpler, less-expensive model of a coarse-grained electrolyte: the so-called implicit solvent (IS). Here, instead of treating the electrolyte solution atomistically, it is described by a continuum model, which includes the dielectric and electrolyte screening.[29] While this approach lowers the computational effort significantly, the use of IS requires parametrization of model aspects such as the solvation cavity and the dielectric response.[35] For the IS, we rely on the SCCS model[36,37] with solvent parameters from Hörmann et al.[10,38] as implemented in the Quantum ENVIRON package.[36]

The energetics of all adsorbate structures is computed with DFT using the PBE functional[39] to treat electronic exchange and correlation. All calculations are performed with the Quantum ESPRESSO package[37,40] and ultrasoft pseudopotentials from the GBRV database (GBRV 1.5),[41] and are managed with the AiiDA-Quantum ESPRESSO pw workflow.[42] The (4×4) supercells employed to model the extended Ag(100) electrode comprise symmetric six layer slabs that are separated by a vacuum region of 18.5 Å. Keeping the two innermost slab layers frozen at the optimized bulk distance, all structures are fully relaxed to energy and force thresholds below 1.0×10^{-4} Ry and 5.0×10^{-3} Ry/bohr, respectively. Convergence tests indicate that at the employed computational settings (`ecutwfc` = 45 Ry, `ecutrho` = 360 Ry for the plane wave basis set, $(4 \times 4 \times 1)$ gamma-centered k-point grid) the Br adsorption energies, E_{ads}, are converged to within 0.01 eV, with further details on the DFT calculations provided in the Supporting Information.

With respect to the most relevant properties of the studied system, namely, the work function and the adsorption energies, previous work indicates a better performance of the PBE functional as compared to other semilocal functionals.[43,44] Nonetheless, PBE is known to underestimate formation energies of bulk halides by ∼0.4 eV[45,46] and similar errors are reported for the adsorption energies of according species.[44,47] This generally needs to be kept in mind when judging predicted absolute CV peak positions, and we will return to this point below. Fortunately, this uncertainty does not directly affect the here first aspired relative comparison of different computational approaches to the CV modeling that we consistently all base on the same PBE energetics.

3.3. Ab Initio Thermodynamics. To evaluate the stability of adsorbate structures at applied electrode potential and experimental ion concentrations, we resort to two established electrochemical ab initio thermodynamics approaches.[16,27,48−51]

The most prominent method, the computational hydrogen electrode (CHE) approach,[16] proved successful in replicating experimental CV peaks for a variety of systems.[9,52,53] As shown in detail in ref 17, the CHE can be interpreted as a first order approximation of the fully grand canonical (FGC) energetics, only necessitating the energetics without electronic (and thus electrolyte) excess charges within the simulation cell, which we will simply refer to as potential of zero charge (PZC) conditions. Thus, the CHE can be evaluated in both vacuum and IS environments.[29,54−56] Note, here and in previous

https://doi.org/10.1021/acs.jctc.3c00957
J. Chem. Theory Comput. 2023, 19, 8815−8825

works,[17] the term CHE refers only to its common application at the so-defined PZC conditions, but not to its application at finite interfacial field or at finite, constant electronic excess charge.

In CHE, the stability of a structure α with N_{Br}^{α} adsorbed Br atoms and N_{sites}^{α} possible adsorption sites (and correspondingly a coverage $\theta_{Br}^{\alpha} = N_{Br}^{\alpha}/N_{sites}^{\alpha}$) is given by the excess energy per surface site

$$g_{exc}^{\alpha,CHE} = \frac{1}{N_{sites}^{\alpha}}[G_{surf,0}^{\alpha} - G_{Ag,0}^{bulk}] - \theta_{Br}^{\alpha}\mu_{Br}, \tag{3}$$

with G here and henceforth referring to Gibbs free energies and the subscript 0 to an evaluation at the PZC. $G_{surf,0}^{\alpha}$ ($G_{Ag,0}^{bulk}$) is correspondingly the Gibbs free energy of the surface structure α (Ag bulk), and μ_{Br} is the joint chemical potential for a charge-neutral Br species (Br = $Br^- - e^-$) with

$$\mu_{Br} = \tilde{\mu}_{Br^-} - \tilde{\mu}_{e^-} = \frac{1}{2}G_{Br_2(g)} + k_B T \ln c_{Br^-} + e(\phi_E - \phi_{Br}^{ref}). \tag{4}$$

Here, $G_{Br_2(g)}$ is the Gibbs free energy of a $Br_2(g)$ gas-phase molecule, c_{Br^-} is the ion concentration in mol/L, and ϕ_{Br}^{ref} is the equilibrium potential for $Br_2(g)$ evolution at standard conditions. To reference the resulting DFT energies to the experimental Ag/AgCl reference electrode, we shift the values of ϕ_E using the literature experimental value of $\phi_{E,ref}^{Ag/AgCl} = 4.637$ V,[57] i.e.,

$$\phi_E = \phi_E^{vs\ Ag/AgCl} + \phi_{E,ref}^{Ag/AgCl}. \tag{5}$$

Simple substitution of the Gibbs free energy expressions above with DFT energetics ($G \to E$) ignores vibrational zero-point and temperature effects, which can lead to sizable errors.[51] To include these efficiently, we reexpress $g_{exc}^{\alpha,CHE}$ as[10]

$$g_{exc}^{\alpha,CHE} = g_{exc}^{clean} + \theta_{Br}^{\alpha}G_{ads}^{\alpha}, \tag{6}$$

where g_{exc}^{clean} is the site-normalized cost of creating a clean interface

$$g_{exc}^{clean} = \frac{1}{N_{sites}}[G_{surf,0}^{clean} - G_{Ag,0}^{bulk}], \tag{7}$$

and G_{ads}^{α} is the coverage-normalized adsorption energy for a configuration α

$$G_{ads}^{\alpha} = \frac{1}{N_{Br}^{\alpha}}[G_{surf,0}^{\alpha} - G_{surf,0}^{clean}] - \mu_{Br}. \tag{8}$$

As vibrational free energy differences between metallic slabs and equally sized metallic bulk materials largely cancel, we can then approximate g_{exc}^{clean} (eq 7) with differences in DFT energies. A similar reasoning applies to the energy differences in eq 8, which is why it is sufficient to only consider the vibrational modes of N_{Br}^{α} adsorbates and of the Br_2 gas-phase molecule to estimate G_{ads}^{α} sufficiently accurate, see the Supporting Information for details of these vibrational calculations.

As the CHE approximation considers only charge-neutral surfaces (i.e., surfaces at their respective PZC), it intrinsically omits higher order potential dependencies of the interfacial energetics,[27,38] thereby also a priori fixing the electrosorption valency to its nominal value, $l_{Br} = -1$. These higher order effects can be approximately included by using an efficient IS model, which allows charging the interfacial system. Explicitly evaluating the energetics at applied potential conditions[38] then yields theoretical predictions for l_{Br}.[27] In fact, the CV current expression of eq 1 emerges naturally from such FGC energetics[10,27] without adjustable parameters.

Further analysis of the FGC energetics shows that many of the aforementioned higher order dependencies in the potential are already captured by performing a second order Taylor expansion in the potential.[17] The second order term can be interpreted as the energy contribution due to DL charging as well as due to geometric relaxation,[58,59] which is not present in the CHE approximation.[10,38] The expression of the free energy within this CHE+DL framework is[38]

$$g_{exc}^{\alpha,CHE+DL} = g_{exc}^{\alpha,CHE} - \frac{1}{2}A_{site}C_0^{\alpha}\left(\phi_E - \phi_0^{\alpha}\right)^2 \tag{9}$$

where A_{site} is the adsorption site-normalized surface area of the substrate, C_0^{α} is the capacitance, and ϕ_0^{α} is the PZC of structure α (i.e., its work function).

In contrast to performing explicit calculations at each studied potential, the CHE+DL method allows one to capture the dominant potential dependencies in IS environments while necessitating only a few additional DFT evaluations at nonzero surface charge to obtain C_0^{α}.

While principally an approximation, in practice the second order CHE+DL method yields identical results as potential calculations in common IS models, where the electronic surface charges are varied explicitly.[17,58,59] This is due to the very simple charge−potential relations within these IS models, which result in potential-independent interfacial capacitances.

Please see the Supporting Information for a complete listing of all DFT calculated thermodynamic properties, including G_{ads}^{α} and corresponding g_{exc}, the work functions ϕ_0, and the implicit model determined C_0^{α} as obtained from explicitly determining the charge-versus-potential relation.

3.4. Statistical Sampling. Knowing the thermodynamic stability of the set of adsorption structures α allows us to derive macroscopic observables by an appropriate statistical mechanics treatment that evaluates the configurational entropic contributions. Here, we follow two routes, namely, using the previously introduced approach based on mean-field theory (MFT)[10] and an approach based on more rigorous lattice GC-MC sampling.[14,21,60]

Equilibrium coverages within MFT are determined via the construction of an approximate free energy landscape $g^{\theta_{Br},MFT}$ as a function of θ_{Br} and subsequent minimization in θ_{Br}-space. In previous work,[10] we only considered a single, high-symmetry composition α at each coverage and determined $g^{\theta_{Br},MFT}$ by interpolating $g_{exc}^{\theta_{Br},CHE(+DL)}$ in θ_{Br} and adding an ideal-solution-like entropy term. Having sampled the full configuration space of the (4 × 4) supercell, we here construct $g^{\theta_{Br},MFT}$ identically, but instead explicitly average over all configurations α at given θ_{Br} according to

$$g_{exc}^{\theta_{Br},CHE(+DL)} = \sum_{\alpha|\theta_{Br}^{\alpha}=\theta_{Br}} p^{\alpha} g_{exc}^{\alpha,CHE(+DL)} \quad \text{with} \tag{10}$$

$$p^{\alpha} = \frac{n_{\alpha}}{\sum_{\alpha|\theta_{Br}^{\alpha}=\theta_{Br}} n_{\alpha}}. \tag{11}$$

Here, n_{α} is the statistical weight (multiplicity) of each symmetry-inequivalent structure α as determined by enumeration and symmetry reduction of all structures within the (4 ×

https://doi.org/10.1021/acs.jctc.3c00957
J. Chem. Theory Comput. 2023, 19, 8815−8825

4) cell. In the high-temperature and large-cell limit, this explicit average is consistent with the ideal-solution-like entropy term within MFT.[61]

In our GC-MC calculations, we map the adsorption patterns α on the 2D square lattice of the Ag(100) surface and fit the energetics $g_{\mathrm{exc}}^{\alpha,\mathrm{CHE(+DL)}}$ under given conditions (ϕ_{E}, c_{Br^-}) with a two-body cluster expansion (2b-CE), using the ICET python package,[62] in a similar approach to ref 63. Next, we run the GC-MC simulations in a (18×18) 2D square lattice to obtain macroscopic averages for the coverage θ_{Br} under the respective conditions. More computational details and convergence tests are provided in the Supporting Information.

Finally, to derive CV currents from eq 1, we set $l_{\mathrm{Br}} = -1$ for the CHE & MFT and CHE & GC-MC calculations, and use the analytic expression for l_{Br} from ref 10 for the CHE+DL and MFT analysis. For the CHE+DL & GC-MC analysis, we determine l_{Br} via eq 2 with differential coverage changes at points (ϕ_{E}, c_{Br^-}) evaluated numerically by performing additional GC-MC simulations at slightly altered conditions (ϕ_E + $\mathrm{d}\phi_{\mathrm{E}}$, c_{Br^-} + $\mathrm{d}c_{\mathrm{Br}^-}$), cf. Supporting Information for details.

4. RESULTS

In the subsequent sections, we assess the effectiveness of various modeling steps, as illustrated in Figure 2. Following the principle of Occam's razor, we start from the most simple and computationally most efficient approach: vacuum-DFT calculations, CHE thermodynamics, and MFT statistical sampling. By improving the statistical sampling and gradually incorporating solvation and capacitive effects (at the level of an implicit solvent model), we carefully examine their influence on the overall outcomes, weighing their potential for improvement against the added complexity and cost that they introduce. We always employ the same scan rate and ion concentration as in the normalized experimental CVs of Figure 1, so that the results can be directly benchmarked against this reference.

4.1. Vacuum Energetics and CHE: Influence of the Statistical Sampling. *4.1.1. Robustness of the MFT Approach.* We begin by comparing the performance of MFT and lattice GC-MC. As the influences of the statistical sampling method are largely independent of the ab initio thermodynamics modeling and the employed solvation model, we expect the resulting insights to then also transfer to the approaches incorporating the solvation and capacitive effects discussed below. Compared to the explicit GC-MC sampling, MFT seems more straightforward and computationally less demanding at first sight. However, as the MFT approach requires representing the coverage-dependent interfacial energetics $g_{\mathrm{exc}}(\theta_{\mathrm{Br}})$ as a continuous function, it necessarily involves an interpolation of the discrete first-principles data available at the coverages that can be accessed in the employed finite-size surface unit-cell. Here, this is a (4×4) cell which correspondingly provides DFT energetic data at 1/16 ML coverage steps.

Due to the strong, repulsive interactions between Br adsorbates, the interpolation method needs to be of a higher order than, for instance, the linear interpolations that have previously been employed for the modeling of CVs of H-electrosorption on Pt.[9,64,65] To examine the sensitivity of the MFT approach on the employed interpolation method, we therefore compare third order polynomial (POL), Gaussian process regression (GPR, see the Supporting Information for more details), and cubic splines (SPL) interpolation. The resulting CVs are shown in Figure 3 and are discomfortingly

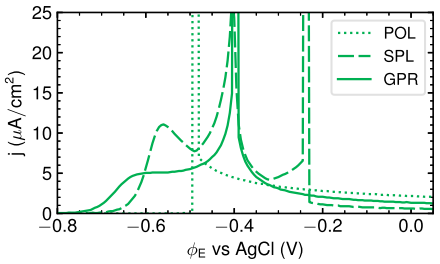

Figure 3. Effect of the employed interpolation method on CVs modeled with vacuum energetics, CHE, and MFT. POL = third order polynomial interpolation, SPL = cubic spline interpolation, and GPR = Gaussian process regression. Only the GPR interpolation recovers the double peak structure observed experimentally; cf. Figure 1.

different. While all three methods yield a CV centered around ∼−0.5 V versus AgCl, this CV has a widely differing shape consisting of one, two, and three subpeaks for the POL, GPR, and SPL interpolation, respectively.

This finding is easily explained as flexible interpolation methods can lead to nonconvex regions in the $g_{\mathrm{exc}}(\theta_{\mathrm{Br}})$ function that result in discontinuous coverage changes as a function of the applied potential and thus sharp spikes in the predicted CV.[27] The POL interpolation introduces no such region, while the more flexible methods GPR and SPL introduce one and two such regions, respectively. We are thus generally faced with the dilemma that a certain flexibility in the interpolation is required to appropriately capture the coverage dependence of $g_{\mathrm{exc}}(\theta_{\mathrm{Br}})$, while too much flexibility can quickly lead to artifacts in the given finite DFT data. In principle, this may, of course, be remedied by increasing the θ_{Br}-resolution of the DFT data. Yet, this would involve the use of larger surface unit-cells and more individual calculations, at concomitant strongly increased computational costs. At the present resolution, the GPR is the only method that recovers the experimentally observed double-peak structure of the CV, cf. Figure 1. We ascribe this to the controllable smoothness of the regressive properties of this method; see the Supporting Information for details, but note that the recovery of the experimental CV shape is only achieved after a careful tuning of the corresponding hyper-parameter. Even though the interpolation step is thus also critical for GPR interpolation, we focus on this method in the following.

A second issue for the interpolation method is its robustness to possible noise in the DFT data. Such noise can arise from multiple sources, ranging from not fully converged DFT calculations to finite ab initio molecular dynamics sampling in explicit solvation models.[66] Figure 4 shows corresponding CVs in which the underlying $G_{\mathrm{ads}}^{\alpha}(\theta_{\mathrm{Br}})$ (i.e., the discrete data before interpolation) were distorted with white noise of varying strength (see the Supporting Information for more noise levels). Again a quite discomforting sensitivity is deduced in which already small noise levels induce strong shape changes dominated by spikes due to erratic coverage discontinuities. To put this into perspective, we also include in Figure 4 the CVs that are obtained when using the same distorted data as the basis for a GC-MC sampling. Specifically, we here used a 2b-CE with the interaction cutoff set to 4.3 Å, such that the expansion includes on-site energy and first and second NN interactions that are parametrized with the DFT data; cf. Supporting Information for more details on and convergence of the 2b-CE. With the exception of overall CV shifts, the GC-MC CVs retain their peak shape much better under the

https://doi.org/10.1021/acs.jctc.3c00957
J. Chem. Theory Comput. 2023, 19, 8815−8825

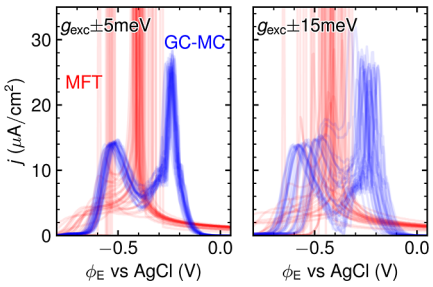

Figure 4. Sensitivity analysis of GPR-interpolated MFT- (red) and GC-MC (blue) CVs (using vacuum energetics and CHE) to white noise in the DFT data. Plotted are 30 CVs each, in which the underlying $g_{exc}(\theta_{Br})$ DFT data were distorted by random errors in the range (left) ± 5 meV and (right) ± 15 meV.

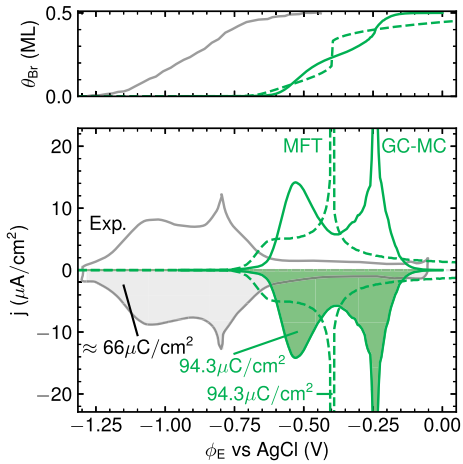

Figure 5. Comparison of the best-practice GPR-interpolated MFT (dashed, green line) and GC-MC (solid green line) CV with the normalized experimental CV from Figure 1 (solid, gray line).[15] Both theoretical CVs are based on vacuum energetics and CHE. Also indicated is the total transferred electronic charge obtained from integrating each CV. The top panel shows the corresponding surface coverage. The experimental coverage isotherm is taken from chronocoulometry measurements from Wandlowski et al.[13]

influence of noise, in fact even up to the high noise level shown in Figure 4.

The superior stability of GC-MC likely results from the fact that the noise can only affect the interaction weights of the GC-MC's predetermined Hamiltonian, while it can alter the overall nature of the MFT Hamiltonian. In the present short-range 2b-CE, a change in the adsorption energy shifts only the entire CV peak. The first NN interaction is energetically so unfavorable that any small changes do not affect the essential blocking of NN occupations in the adsorbate lattice. As a result, actual variations in the peak shapes are only introduced by noise-induced variations in the weaker repulsive second NN interaction, where increasing or decreasing values merely stretch or compress the CV, cf. Supporting Information. This limited mapping induces an inherent robustness to errors. To be fair, one should note though that this is gradually lost when increasing the 2b interaction cutoff or including many-body interactions into the CE. As shown in the Supporting Information, we then also obtain somewhat larger distortions of the GC-MC CVs. However, they are never as large as those of the MFT CVs for the same noise level, and we also observe a systematic and rapid convergence of the simulated CVs with respect to an increase in the 2b interaction cutoff. This demonstrates that the robust short-range CE with only first and second NN interactions (interaction cutoff set to 4.3 Å) as in Figure 4 is fully sufficient for the present system and used henceforth as default.

4.1.2. MFT vs GC-MC Sampling. The results of the last subsection reveal that while MFT is an easy and quick approach, its sensitivity to the employed interpolation method and to noise in the DFT data render it nonideal to model CVs with complex peak shapes. This assessment does thereby not even extend to its approximate handling of the configurational entropy. We assess the latter in Figure 5 where we directly benchmark the CVs obtained with the determined best-practice MFT and GC-MC model against the normalized experimental data. Both theoretical CVs are strongly shifted and more compressed compared to the experimental reference. In both methods, the onset of Br electrosorption occurs at ∼−0.6 V versus AgCl and is followed by a shoulder feature consistent with the experimentally observed peak P1 as discussed in Section 2. Similarly, both methods yield a sharper second peak P2 at higher potentials (MFT at −0.4 V vs AgCl, GC-MC at −0.25 V vs AgCl).

In detail, however, the two methods do predict quite different CV shapes, with the MFT approach with its nominally inferior sampling in fact somewhat better reproducing the experimental shape, in terms of both the more humplike character of the P1 peak and the sharp spikelike character of the P2 peak. Yet, with respect to the latter, one can clearly show that this is completely fortuitous. In the GC-MC simulations, the P2 peak arises as expected from a second order disorder−order phase transition of the Br adlayer. Using order parameters appropriate for (2×2) ordering,[67,68] the freezing out of the ordered $c(2 \times 2)$ structure from a previously disordered lattice gas at potentials around P2 can nicely be discerned as shown in the Supporting Information. In fact, the employed short-range CE truncated to first and second NN interactions directly connects to a bulk of work with corresponding model Hamiltonians on square lattices. From such work, the nature of the disorder−order phase transition is well-known. For a site-blocking first NN repulsive interaction, the transition occurs at about 75−80% of the limiting coverage of 0.5 ML.[14,21,25,26,69] Furthermore, this critical coverage θ_c varies only slightly in the presence of longer-range interactions and remains at 80% for a large range of repulsive second NN interaction energies.[69] Fully consistent with this, peak P2 arises at $\theta_c \approx 80\%$ in our GC-MC simulations, and the previously discussed robustness of the simulation results in particular with respect to the P2 part of the CV directly correlates with the known robust and universal nature of this phase transition.

In contrast, MFT is by construction completely agnostic to such disorder−order physics. Here, the P2 peak derives simply from a discontinuous jump in θ_{Br} occurring between 0.20 and 0.35 ML, i.e., at 50−70% of the maximum coverage. As already stated, this jump is the result of a nonconvex coverage-dependence of g_{exc}, and thus depends sensitively on the details of the DFT data points and the interpolation method. The good agreement of the MFT P2 peak shape is thus a prime example of right for wrong reasons, and we will see next that the worse prediction obtained for the superior GC-MC sampling is in fact the consequence of the hitherto still lacking treatment of solvation and capacitive effects.

4.2. GC-MC & CHE: Solvent Stabilization. In view of the inherent deficiencies of the MFT sampling, we concentrated

https://doi.org/10.1021/acs.jctc.3c00957
J. Chem. Theory Comput. 2023, 19, 8815−8825

our ensuing analysis on GC-MC sampling. Apart from the differences in the overall CV shape with respect to the experimental reference, a second discrepancy of the aforementioned GC-MC CV obtained with vacuum energetics and the CHE was an overall offset by ≈0.5 V. Such a shift to more anodic potentials might well be due to the lack of solvent stabilization in the hitherto employed vacuum energetics. In our next analysis step, we correspondingly still stay within the CHE, but now employ the DFT energetics obtained with the implicit solvation model. Figure 6 compares the corresponding

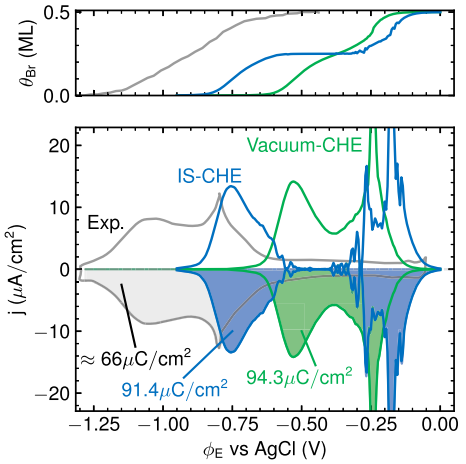

Figure 6. Same as Figure 5, but now comparing GC-MC and CHE CVs based on vacuum energetics (solid, green line) and implicit solvation (IS) energetics (solid, blue line) with the normalized experimental CV from Figure 1 (solid, gray line).[15] Also indicated is the total transferred electronic charge obtained from integrating each CV. The top panel shows the corresponding surface coverage. The experimental coverage isotherm is taken from chronocoulometry measurements from Wandlowski et al.[13]

CV with that obtained with vacuum energetics and the experimental reference. Indeed, the onset of the implicit-solvent CV shifts to lower potentials, reflecting a stabilization of the respective low-coverage adsorbate configurations by the solvent model. However, this is accompanied by an opposite slight upward shift of the higher-coverage P2-peak part of the CV. As a result, the overall CV becomes much broader than the experimental reference, and de facto separates into two parts.

A direct comparison of the coverage-dependent adsorption energies in a vacuum and IS in the top panel in Figure 7 points to the origin of this separation. While $G_{ads}^{CHE}(\theta_{Br})$ at low coverages are stabilized by the solvent model by ∼250 meV per Br adsorbate relative to the vacuum energetics, the IS-induced stabilization diminishes with increasing coverage, becoming negligible at the highest coverage of θ_{Br} = 0.5 ML. In the short-range 2b-CE, this translates to a decrease in the onsite term of 203 meV and an doubling of the repulsive second NN interaction term from 60 meV in vacuum to 135 meV in implicit solvation. Overall, this then spreads the coverage isotherm as seen in Figure 6 and concomitantly the CV. The diminishing stabilization in turn is a direct consequence of the implicit solvent representation in the form of a dielectric continuum beyond a solvation cavity defined by a threshold electron density.[36] As apparent from Figure 8, at low coverage this cavity extends to close to the surface in the large clean parts of the surface between the dilute Br adsorbates. In

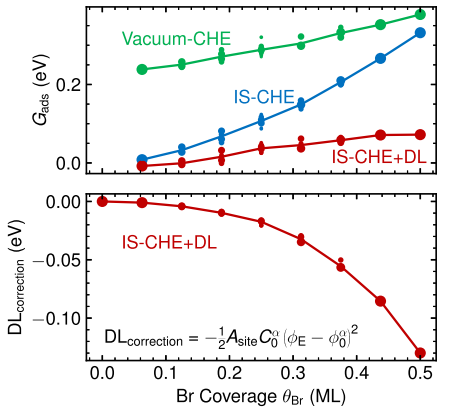

Figure 7. Adsorption energy G_{ads} for all DFT-calculated configurations α plotted against their respective Br coverage θ_{Br}, evaluated at ϕ_E = −0.8 V vs AgCl (top panel), the center of the experimental CV. The size of the scatter points corresponds to p^{α} (eq 11). We show CHE values for vacuum (green) and implicit solvent energetics (blue) as well as the CHE+DL values within the implicit solvent model (red). The correction term introduced by the CHE+DL scheme ($DL_{correction}$) is shown in the bottom panel. In both figures, the lines correspond to the weighted average values for each unique coverage.

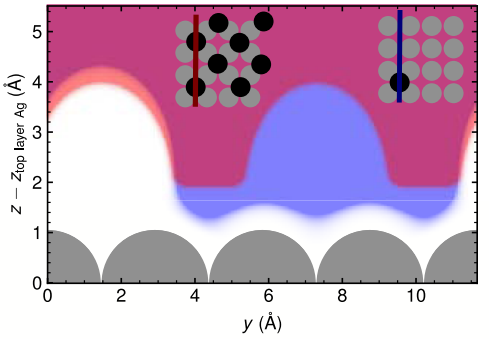

Figure 8. Side view of the solvation cavity of the implicit solvation model for a low-coverage $p(4 \times 4)$ (blue) and a high-coverage $c(2 \times 2)$ (red) Br adsorbate layer. The insets explain the position of the vertical cut above the surface. In the case of a low-coverage adsorbate layer, the dielectric medium extends much closer to the surface between the adsorbates, thus enabling higher solvent stabilization due to screening.

contrast, this is no longer possible at the small spacing between the Br adsorbates at the highest coverage. The stabilization in the IS model results from a simple screening of the repulsive electrostatic interactions between the Br adsorbates by the dielectric medium. With this medium being able to encapsulate the Br adsorbates much better at low coverages, a higher stabilization consequently arises as compared to the high-coverage case where this is no longer possible (as the solvent cannot penetrate between the adsorbates anymore). Even though the IS model is a coarse representation of the true solvation environment, this varying screening and concomitantly differing degrees of solvent stabilization should in principle be the correct physics. As in the case with the sampling before, we thus again arrive at the result that a nominally better modeling does not directly lead to an improved CV observable.

4.3. GC-MC & CHE+DL: Capacitive Charging Effects. The last missing piece in the modeling hierarchy is the consideration of capacitive charging effects via the CHE+DL

https://doi.org/10.1021/acs.jctc.3c00957
J. Chem. Theory Comput. 2023, 19, 8815−8825

approach. Figure 9 correspondingly compares the simulated GC-MC CV based on implicit solvation energetics at the CHE

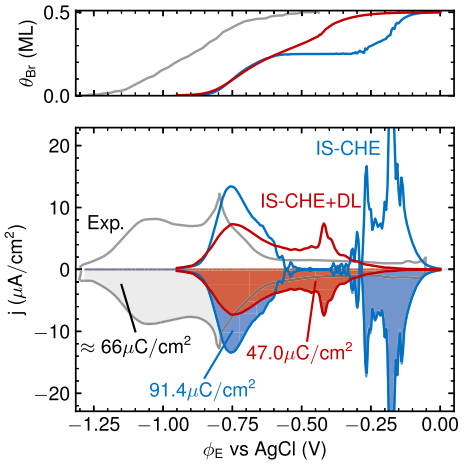

Figure 9. Same as Figures 5 and 6, but now comparing GC-MC & implicit solvation CVs based on CHE (solid, blue line) and implicit solvation energetics (solid, red line) with the normalized experimental CV from Figure 1 (solid, gray line).[15] Also indicated is the total transferred electronic charge obtained from integrating each CV. The top panel shows the corresponding surface coverage. The experimental coverage isotherm is taken from chronocoulometry measurements from Wandlowski et al.[13]

and CHE+DL levels with the experimental reference. Remarkably, the second order inclusion of the electrode potential largely reverts the excessive CV broadening observed previously when switching from vacuum to implicit solvation energetics at the CHE level, while at the same time, leaving the onset potential of the CV unchanged. As a result, a CV shape highly reminiscent of the experimental CV is again obtained, but with the entire CV now also located at more cathodic potentials closer to this reference.

This result can be rationalized by analyzing the quadratic DL correction term $-\frac{1}{2}A_{site}C_0^{\theta_{Br}}(\phi_E - \phi_0^{\theta_{Br}})^2$ that is introduced at this level of theory. Figure 7 shows the coverage dependence of this term when approximately evaluating it for $\phi_E = -0.8$ V vs AgCl and thus at a potential that roughly corresponds to the center of the experimental CV. At such relevant potentials, the term becomes increasingly negative with increasing coverage and therefore effectively cancels the increased positive slope of the $\theta_{Br}G_{ads}^{CHE}$ CHE-term upon changing to implicit solvation energetics, cf. Figure 7. As shown in Figure 7, this leads to $G_{ads}^{IS\text{-}CHE+DL}$ exhibiting almost the same slope as that of $G_{ads}^{vacuum\text{-}CHE}$. In other words, the fortuitous agreement of the shape of the CHE plus vacuum energetics CV with experiment was the result of a cancellation of errors introduced by the simultaneously missing solvation and capacitive charging effects.

However, the CHE+DL approach not only improves the overall peak shape and absolute position of the CV. It also significantly reduces the total transferred electronic charge σ_{Br}, i.e., the integrated area under the CV, as well as changes the relative height of the P1 and P2 peaks. Both of these changes again improve the comparison to the experimental reference. In particular, σ_{Br} was consistently overestimated within all previous modeling approaches, cf. Figures 5, 6, and 9, and is now in much better agreement with the experiment. Both of these effects arise from the electrosorption valency $l_{Br}(\theta_{Br}, \phi_E)$ that scales the overall CV, cf. eq 1, and that in the CHE+DL approach can now take values less negative than the nominal charge of −1.[38] As shown in the Supporting Information, the CHE+DL l_{Br} is in fact not constant, but increases almost linearly from −0.7 to −0.45 over the potential window (aka coverage) of the CV and falls thus into the range estimated for the electrosorption valency from the experimental data, cf. Section 2. This potential dependence of l_{Br} then alters the relative heights of the P1 and P2 peaks, as less charge is transmitted per adsorbate at lower than at higher coverages. It is also only this noninteger value of l_{Br} that leads to the non-Nernstian potential shift of the P2 peak with Br^- concentration reported experimentally.[13]

Overall and gratifyingly, it is thus indeed the CV modeled at the nominally best level of theory that achieves the best agreement with the experimental reference, i.e., a CV obtained by GC-MC sampling, energetics accounting for solvation effects at least at the level of an implicit solvation model, as well as considering capacitive charging effects to the second order. In fact, considering that we have focused only on computationally efficient approaches that in many respects are still effective, prominently the description of the solvation environment by a mere dielectric continuum, this agreement down to width, shape, and integrated area of the CV is quite impressive. What remains as the largest discrepancy is the overall potential shift of about ∼0.3 V of the predicted CV versus the experimental data. We ascribe much of this difference to the employed semilocal PBE DFT functional and support this assignment with a recalculation of all vacuum DFT energetics with the revPBE functional, cf. Supporting Information for details. We obtain G_{ads} for all configurations α that are predominantly shifted by about ∼+0.15 eV as compared to the corresponding PBE values. Consequently, while the on-site term of a short-range 2b-CE based on these energetics becomes less stable by ∼0.15 eV, the first and second NN interactions remain unchanged. Obviously, the entire analysis of the last sections would thus hold in an analogous way for this CE, just with the entire simulated CVs shifted by ∼0.15 V to more cathodic potentials and thus even further away from the experimental reference. This agrees with the general expectation of an even weaker binding at the revPBE level and the knowledge that already the PBE underestimates the binding of halides.[44−47] Of course, just testing one other semilocal functional does not do justice to the wealth of approximate DFT energetics that can in principle be obtained. Nevertheless, we believe that the provided singular example illustrates that this uncertainty in the energetics may prominently lead to overall shifts of the simulated CV. As such, the approximate DFT energetics are in our view the most likely candidate to explain the remaining discrepancy of the GC-MC CHE+DL CV based on implicit solvation energetics with respect to the experimental reference.

5. SUMMARY AND CONCLUSIONS

In this benchmark study, we have systematically analyzed prominent choices in the simulation workflow for thermodynamic CVs using Br electrosorption at a model Ag(100) electrode as a representative showcase. Focusing on computationally efficient, prevalent approaches, we analyzed the influence of an approximate account of the solvation environment in form of energetics calculated within an implicit solvation model, of an ab initio thermodynamics description that incorporates capacitive charging up to second order in the

https://doi.org/10.1021/acs.jctc.3c00957
J. Chem. Theory Comput. 2023, 19, 8815−8825

potential, as well as of a grand-canonical Monte Carlo sampling that explicitly evaluates configurational entropic effects in the adlayer. As a crucial insight, we observed an intricate error cancellation when several of these aspects were treated more approximately. A good agreement of a simulated CV with experimental data can thus not be taken uncritically as evidence that the employed level of theory was sufficient.

At the nominally best level of theory considered in this study (GC-MC sampling, implicit solvation energetics, and CHE +DL thermodynamics), we obtain a gratifying essentially quantitative agreement of the simulated CV with experimental reference data. The analysis provided suggests that this is the result of an appropriate description of key physics of this system, in particular, a coverage-dependent solvation stabilization due to a varying capability of the solvent to penetrate the adlayer and the disorder−order phase transition of the Br adlayer at higher coverages. Nevertheless, in view of the error cancellations observed at the lower levels of theory, this agreement should be scrutinized further in future work. Most prominently, we envision explicit electrolyte approaches as the next frontier that would provide the most valuable feedback on the true reliability of the implicit solvation method employed here employed implicit solvation method. Specifically, we hereby refer to both the parametrization of the implicit solvation model and its fundamental deficiencies in appropriately describing H-bonding networks and other directed solvent interactions at all. We consider the wealth of experimental CVs available for this system as an opportunity to systematically analyze such aspects with respect to a firm reference.

■ ASSOCIATED CONTENT

Supporting Information

The Supporting Information is available free of charge at https://pubs.acs.org/doi/10.1021/acs.jctc.3c00957.

Digitalization of the experimental CVs, structure sampling, DFT calculations, mean-field theory, lattice grand-canonical Monte-Carlo, sensitivity analysis, order parameter and structure factor calculations, and more detailed data on the inclusion of double layer effects (PDF)

■ AUTHOR INFORMATION

Corresponding Author

Nicolas G. Hörmann − *Fritz-Haber-Institut der Max-Planck-Gesellschaft, D-14195 Berlin, Germany;* orcid.org/0000-0001-6944-5575; Email: hoermann@fhi-berlin.mpg.de

Authors

Nicolas Bergmann − *Fritz-Haber-Institut der Max-Planck-Gesellschaft, D-14195 Berlin, Germany;* orcid.org/0000-0001-7586-2471

Karsten Reuter − *Fritz-Haber-Institut der Max-Planck-Gesellschaft, D-14195 Berlin, Germany;* orcid.org/0000-0001-8473-8659

Complete contact information is available at: https://pubs.acs.org/10.1021/acs.jctc.3c00957

Funding

Open access funded by Max Planck Society.

Notes

The authors declare no competing financial interest.

■ ACKNOWLEDGMENTS

The authors thank S. Beinlich and T. Eggert for useful discussions and suggestions during this project, as well as V. J. Bukas and H. Oschinski for their contributions to the development of this paper. The authors acknowledge funding and support from the German Research Foundation (DFG) under Germany's Excellence Strategy—EXC 2089/1-390776260 (e-conversion) and financial support through the EuroTech Postdoc Programme, which is cofunded by the European Commission under its framework programme Horizon 2020 and grant agreement number 754462. All computations were performed on the HPC system Raven at the Max Planck Computing and Data Facility, which we gratefully acknowledge.

■ REFERENCES

(1) Bard, A. J.; Zoski, C. G. Voltammetry Retrospective. *Anal. Chem.* **2000**, *72*, 346−352 A.

(2) Nicholson, R. S. Theory and Application of Cyclic Voltammetry for Measurement of Electrode Reaction Kinetics. *Anal. Chem.* **1965**, *37*, 1351−1355.

(3) Elgrishi, N.; Rountree, K. J.; McCarthy, B. D.; Rountree, E. S.; Eisenhart, T. T.; Dempsey, J. L. A Practical Beginner's Guide to Cyclic Voltammetry. *J. Chem. Educ.* **2018**, *95*, 197−206.

(4) Kissinger, P. T.; Heineman, W. R. Cyclic voltammetry. *J. Chem. Educ.* **1983**, *60*, 702.

(5) Climent, V.; Feliu, J. *In Encyclopedia of Interfacial Chemistry*; Wandelt, K., Ed.; Elsevier: Oxford, 2018; pp 48−74.

(6) Engstfeld, A. K.; Maagaard, T.; Horch, S.; Chorkendorff, I.; Stephens, I. E. L. Polycrystalline and Single-Crystal Cu Electrodes: Influence of Experimental Conditions on the Electrochemical Properties in Alkaline Media. *Chem.—Eur. J.* **2018**, *24*, 17743−17755.

(7) Sheng, W.; Zhuang, Z.; Gao, M.; Zheng, J.; Chen, J. G.; Yan, Y. Correlating hydrogen oxidation and evolution activity on platinum at different pH with measured hydrogen binding energy. *Nat. Commun.* **2015**, *6*, 5848.

(8) Aristov, N.; Habekost, A. Cyclic Voltammetry - A Versatile Electrochemical Method Investigating Electron Transfer Processes. *World J. Chem. Educ.* **2015**, *3*, 115−119.

(9) Karlberg, G. S.; Jaramillo, T. F.; Skúlason, E.; Rossmeisl, J.; Bligaard, T.; Nørskov, J. K. Cyclic Voltammograms for H on Pt(111) and Pt(100) from First Principles. *Phys. Rev. Lett.* **2007**, *99*, 126101.

(10) Hörmann, N. G.; Reuter, K. Thermodynamic Cyclic Voltammograms Based on *Ab Initio* Calculations: Ag(111) in Halide-Containing Solutions. *J. Chem. Theory Comput.* **2021**, *17*, 1782−1794.

(11) Schultze, J.; Vetter, K. Experimental determination and interpretation of the electrosorption valency γ. *J. Electroanal. Chem. Interfacial Electrochem.* **1973**, *44*, 63−81.

(12) Guidelli, R.; Schmickler, W. *In Modern Aspects of Electrochemistry*; Conway, B. E., Vayenas, C. G., White, R. E., Gamboa-Adelco, M. E., Eds.; Springer US: Boston, MA, 2005; pp 303−371.

(13) Wandlowski, T.; Wang, J.; Ocko, B. Adsorption of bromide at the Ag(100) electrode surface. *J. Electroanal. Chem.* **2001**, *500*, 418−434.

(14) Koper, M. T. A lattice-gas model for halide adsorption on single-crystal electrodes. *J. Electroanal. Chem.* **1998**, *450*, 189−201.

(15) Nakamura, M.; Nakajima, Y.; Sato, N.; Hoshi, N.; Sakata, O. Structure of the electrical double layer on Ag(100): Promotive effect of cationic species on Br adlayer formation. *Phys. Rev. B: Condens. Matter Mater. Phys.* **2011**, *84*, 165433.

(16) Nørskov, J. K.; Rossmeisl, J.; Logadottir, A.; Lindqvist, L.; Kitchin, J. R.; Bligaard, T.; Jónsson, H. Origin of the Overpotential for Oxygen Reduction at a Fuel-Cell Cathode. *J. Phys. Chem. B* **2004**, *108*, 17886−17892.

(17) Hörmann, N. G.; Marzari, N.; Reuter, K. Electrosorption at metal surfaces from first principles. *npj Comput. Mater.* **2020**, *6*, 136.

(18) Engstfeld, A.; Rüth, J.; linuxrider; Hörmann, N. G. *echemdb/echemdb: 0.6.0*, 2023.
(19) Endo, O.; Kiguchi, M.; Yokoyama, T.; Ito, M.; Ohta, T. In-situ X-ray absorption studies of bromine on the Ag(100) electrode. *J. Electroanal. Chem.* **1999**, *473*, 19−24.
(20) Ocko, B. M.; Wang, J. X.; Wandlowski, T. Bromide Adsorption on Ag(001): A Potential Induced Two-Dimensional Ising Order-Disorder Transition. *Phys. Rev. Lett.* **1997**, *79*, 1511−1514.
(21) Koper, M. T. Monte Carlo simulations of ionic adsorption isotherms at single-crystal electrodes. *Electrochim. Acta* **1998**, *44*, 1207−1212.
(22) Wang, S.; Rikvold, P. A. Ab initio calculations for bromine adlayers on the Ag(100) and Au(100) surfaces: The $c(2 \times 2)$ structure. *Phys. Rev. B: Condens. Matter Mater. Phys.* **2002**, *65*, 155406.
(23) Mitchell, S.; Brown, G.; Rikvold, P. Dynamics of Br electrosorption on single-crystal Ag(100): a computational study. *J. Electroanal. Chem.* **2000**, *493*, 68−74.
(24) Mitchell, S. J.; Wang, S.; Rikvold, P. A. Halide adsorption on single-crystal silver substrates: dynamic simulations and ab initio density functional theory. *Faraday Discuss.* **2002**, *121*, 53−69.
(25) Persson, B. Ordered structures and phase transitions in adsorbed layers. *Surf. Sci. Rep.* **1992**, *15*, 1−135.
(26) Landau, L. D.; Lifshitz, E. M. *In Statistical Physics*, 3rd ed.; Landau, L. D., Lifshitz, E. M., Eds.; Butterworth-Heinemann: Oxford, 1980; pp 446−516.
(27) Hörmann, N. G.; Reuter, K. Thermodynamic cyclic voltammograms: peak positions and shapes. *J. Phys.: Condens. Matter* **2021**, *33*, 264004.
(28) Koper, M. T.; Lukkien, J. J. Modeling the butterfly: the voltammetry of $(\sqrt{3}\times\sqrt{3})$R30° and p(2×2) overlayers on (111) electrodes. *J. Electroanal. Chem.* **2000**, *485*, 161−165.
(29) Ringe, S.; Hörmann, N. G.; Oberhofer, H.; Reuter, K. Implicit Solvation Methods for Catalysis at Electrified Interfaces. *Chem. Rev.* **2022**, *122*, 10777−10820.
(30) Dudzinski, A. M.; Diesen, E.; Heenen, H. H.; Bukas, V. J.; Reuter, K. First Step of the Oxygen Reduction Reaction on Au(111): A Computational Study of O_2 Adsorption at the Electrified Metal/Water Interface. *ACS Catal.* **2023**, *13*, 12074−12081.
(31) Le, J.-B.; Chen, A.; Li, L.; Xiong, J.-F.; Lan, J.; Liu, Y.-P.; Iannuzzi, M.; Cheng, J. Modeling Electrified Pt(111)-H_{ad}/Water Interfaces from Ab Initio Molecular Dynamics. *JACS Au* **2021**, *1*, 569−577.
(32) Deißenbeck, F.; Freysoldt, C.; Todorova, M.; Neugebauer, J.; Wippermann, S. Dielectric Properties of Nanoconfined Water: A Canonical Thermopotentiostat Approach. *Phys. Rev. Lett.* **2021**, *126*, 136803.
(33) Meng, A. C.; Cheng, J.; Sprik, M. Density Functional Theory Calculation of the Band Alignment of (1010) $In_xGa_{1-x}N$/Water Interfaces. *J. Phys. Chem. B* **2016**, *120*, 1928−1939.
(34) Hörmann, N. G.; Guo, Z.; Ambrosio, F.; Andreussi, O.; Pasquarello, A.; Marzari, N. Absolute band alignment at semiconductor-water interfaces using explicit and implicit descriptions for liquid water. *npj Comput. Mater.* **2019**, *5*, 100.
(35) Schwarz, K.; Sundararaman, R. The electrochemical interface in first-principles calculations. *Surf. Sci. Rep.* **2020**, *75*, 100492.
(36) Andreussi, O.; Dabo, I.; Marzari, N. Revised self-consistent continuum solvation in electronic-structure calculations. *J. Chem. Phys.* **2012**, *136*, 064102.
(37) Giannozzi, P.; Andreussi, O.; Brumme, T.; Bunau, O.; Buongiorno Nardelli, M.; Calandra, M.; Car, R.; Cavazzoni, C.; Ceresoli, D.; Cococcioni, M.; Colonna, N.; et al. Advanced capabilities for materials modelling with Quantum ESPRESSO. *J. Phys.: Condens. Matter* **2017**, *29*, 465901.
(38) Hörmann, N. G.; Andreussi, O.; Marzari, N. Grand canonical simulations of electrochemical interfaces in implicit solvation models. *J. Chem. Phys.* **2019**, *150*, 041730.
(39) Perdew, J. P.; Burke, K.; Ernzerhof, M. Generalized Gradient Approximation Made Simple. *Phys. Rev. Lett.* **1996**, *77*, 3865−3868.
(40) Giannozzi, P.; Baroni, S.; Bonini, N.; Calandra, M.; Car, R.; Cavazzoni, C.; Ceresoli, D.; Chiarotti, G. L.; Cococcioni, M.; Dabo, I.; et al. QUANTUM ESPRESSO: a modular and open-source software project for quantum simulations of materials. *J. Phys.: Condens. Matter* **2009**, *21*, 395502.
(41) Garrity, K. F.; Bennett, J. W.; Rabe, K. M.; Vanderbilt, D. Pseudopotentials for high-throughput DFT calculations. *Comput. Mater. Sci.* **2014**, *81*, 446−452.
(42) Huber, S. P. Automated reproducible workflows and data provenance with AiiDA. *Nat. Rev. Phys.* **2022**, *4*, 431−432.
(43) Schimka, L.; Harl, J.; Stroppa, A.; Grüneis, A.; Marsman, M.; Mittendorfer, F.; Kresse, G. Accurate surface and adsorption energies from many-body perturbation theory. *Nat. Mater.* **2010**, *9*, 741−744.
(44) Schmidt, P. S.; Thygesen, K. S. Benchmark Database of Transition Metal Surface and Adsorption Energies from Many-Body Perturbation Theory. *J. Phys. Chem. C* **2018**, *122*, 4381−4390.
(45) Friedrich, R.; Usanmaz, D.; Oses, C.; Supka, A.; Fornari, M.; Buongiorno Nardelli, M.; Toher, C.; Curtarolo, S. Coordination corrected ab initio formation enthalpies. *npj Comput. Mater.* **2019**, *5*, 59.
(46) Wang, A.; Kingsbury, R.; McDermott, M.; Horton, M.; Jain, A.; Ong, S. P.; Dwaraknath, S.; Persson, K. A. A framework for quantifying uncertainty in DFT energy corrections. *Sci. Rep.* **2021**, *11*, 15496.
(47) Wellendorff, J.; Silbaugh, T. L.; Garcia-Pintos, D.; Nørskov, J. K.; Bligaard, T.; Studt, F.; Campbell, C. T. A benchmark database for adsorption bond energies to transition metal surfaces and comparison to selected DFT functionals. *Surf. Sci.* **2015**, *640*, 36−44.
(48) Reuter, K. Ab initio thermodynamics and first-principles microkinetics for surface catalysis. *Catal. Lett.* **2016**, *146*, 541−563.
(49) Scheffler, M. *In Physics of Solid Surfaces 1987*; Koukal, J., Ed.; *Stud. Surf. Sci. Catal.*; Elsevier, 1988; Vol. *40*, pp 115−122.
(50) Reuter, K.; Scheffler, M. Composition, structure, and stability of RuO_2(110) as a function of oxygen pressure. *Phys. Rev. B: Condens. Matter Mater. Phys.* **2001**, *65*, 035406.
(51) Rogal, J.; Reuter, K. *Ab Initio Atomistic Thermodynamics for Surfaces: A Primer*, 2007.
(52) Tiwari, A.; Heenen, H. H.; Bjørnlund, A. S.; Hochfilzer, D.; Chan, K.; Horch, S. Electrochemical Oxidation of CO on Cu Single Crystals under Alkaline Conditions. *ACS Energy Lett.* **2020**, *5*, 3437−3442.
(53) Tiwari, A.; Heenen, H. H.; Bjørnlund, A. S.; Maagaard, T.; Cho, E.; Chorkendorff, I.; Kristoffersen, H. H.; Chan, K.; Horch, S. Fingerprint Voltammograms of Copper Single Crystals under Alkaline Conditions: A Fundamental Mechanistic Analysis. *J. Phys. Chem. Lett.* **2020**, *11*, 1450−1455.
(54) Groß, A.; Sakong, S. Ab Initio Simulations of Water/Metal Interfaces. *Chem. Rev.* **2022**, *122*, 10746−10776.
(55) Dattila, F.; Seemakurthi, R. R.; Zhou, Y.; López, N. Modeling Operando Electrochemical CO2 Reduction. *Chem. Rev.* **2022**, *122*, 11085−11130.
(56) Nitopi, S.; Bertheussen, E.; Scott, S. B.; Liu, X.; Engstfeld, A. K.; Horch, S.; Seger, B.; Stephens, I. E. L.; Chan, K.; Hahn, C.; Nørskov, J. K.; Jaramillo, T. F.; Chorkendorff, I. Progress and Perspectives of Electrochemical CO2 Reduction on Copper in Aqueous Electrolyte. *Chem. Rev.* **2019**, *119*, 7610−7672.
(57) Jordan, J.; Javick, R. A.; Ranz, W. E. Hydrodynamic Voltammetry at Solid Indicator Electrodes. *J. Am. Chem. Soc.* **1958**, *80*, 3846−3852.
(58) Beinlich, S. D.; Kastlunger, G.; Reuter, K.; Hörmann, N. G. Controlled Electrochemical Barrier Calculations without Potential Control. *J. Chem. Theory Comput.* **2023**, *19* (22), 8323−8331.
(59) Beinlich, S. D.; Kastlunger, G.; Reuter, K.; Hörmann, N. G. A theoretical investigation of the grand- and the canonical potential energy surface: the interplay between electronic and geometric response at electrified interfaces. *arXiv* **2023**, 2307.09817v1. [physics.chem−ph]

(60) Mitchell, S.; Brown, G.; Rikvold, P. Static and dynamic Monte Carlo simulations of Br electrodeposition on Ag(100). *Surf. Sci.* **2001**, *471*, 125−142.
(61) Hörmann, N. G.; Groß, A. Phase field parameters for battery compounds from first-principles calculations. *Phys. Rev. Mater.* **2019**, *3*, 055401.
(62) Ångqvist, M.; Muñoz, W. A.; Rahm, J. M.; Fransson, E.; Durniak, C.; Rozyczko, P.; Rod, T. H.; Erhart, P. ICET − A Python Library for Constructing and Sampling Alloy Cluster Expansions. *Adv. Theory Simul.* **2019**, *2*, 1900015.
(63) Weitzner, S. E.; Dabo, I. Voltage-dependent cluster expansion for electrified solid-liquid interfaces: Application to the electrochemical deposition of transition metals. *Phys. Rev. B* **2017**, *96*, 205134.
(64) McCrum, I. T.; Janik, M. J. pH and Alkali Cation Effects on the Pt Cyclic Voltammogram Explained Using Density Functional Theory. *J. Phys. Chem. C* **2016**, *120*, 457−471.
(65) McCrum, I. T.; Janik, M. J. First Principles Simulations of Cyclic Voltammograms on Stepped Pt(553) and Pt(533) Electrode Surfaces. *ChemElectroChem* **2016**, *3*, 1609−1617.
(66) Heenen, H. H.; Gauthier, J. A.; Kristoffersen, H. H.; Ludwig, T.; Chan, K. Solvation at metal/water interfaces: An ab initio molecular dynamics benchmark of common computational approaches. *J. Chem. Phys.* **2020**, *152*, 144703.
(67) Yarnell, J. L.; Katz, M. J.; Wenzel, R. G.; Koenig, S. H. Structure Factor and Radial Distribution Function for Liquid Argon at 85 °K. *Phys. Rev. A* **1973**, *7*, 2130−2144.
(68) Zhang, Y.; Blum, V.; Reuter, K. Accuracy of first-principles lateral interactions: Oxygen at Pd(100). *Phys. Rev. B: Condens. Matter Mater. Phys.* **2007**, *75*, 235406.
(69) Taylor, D. E.; Williams, E. D.; Park, R. L.; Bartelt, N. C.; Einstein, T. L. Two-dimensional ordering of chlorine on Ag(100). *Phys. Rev. B: Condens. Matter Mater. Phys.* **1985**, *32*, 4653−4659.

https://doi.org/10.1021/acs.jctc.3c00957
J. Chem. Theory Comput. 2023, 19, 8815−8825